Journal of Materials Research and Technology 37 (2025) 3729–3738

Contents lists available at ScienceDirect

Journal of Materials Research and Technology

journal homepage: www.elsevier.com/locate/jmrt

# Microstructural evolution and strength-toughness behavior of fire-resistant steel under thermo-mechanical controlled processing

Hyungkwon Park [a], Hyo-Haeng Jo [a], Chiwon Kim [a], Seong Hoon Kim [a], Kyeong-Won Kim [a], Joonoh Moon [b], Hyun-Uk Hong [b], Jun-Ho Chung [c], Bong-Ho Lee [d], Chang-Hoon Lee [a,*]

[a] Extreme Materials Research Institute, Korea Institute of Materials Science, Changwon, Republic of Korea
[b] Department of Materials Science and Engineering, Changwon National University, Republic of Korea
[c] Research & Development (R&D) Center, Hyundai Steel Company, Incheon, 22525, Republic of Korea
[d] Center for Core Research Facilities, Daegu Gyeongbuk Institute of Science and Technology, Republic of Korea

ARTICLE INFO

Handling Editor: Prof. M Meyers

*Keywords:*
Fire-resistant steel
Thermomechanical controlled processing (TMCP)
Bainite
Yield strength
Impact toughness

ABSTRACT

Fire-resistant steels are engineered to retain high strength at elevated temperatures, typically maintaining a yield strength (YS) ratio (600 °C/RT) above 0.67 to prevent sudden structural collapse during fire exposure. Although achieving such strength retention is critical, ensuring sufficient fracture toughness is equally essential for structural reliability. However, toughness behavior in fire-resistant steels has been largely overlooked, particularly in relation to thermomechanical processing. In this study, the influence of thermomechanical controlled processing (TMCP) on the microstructure and mechanical behavior of fire-resistant steel was investigated, with an emphasis on the strength-toughness trade-off. With increasing TMCP conducted below the non-recrystallization temperature ($T_{nr}$), the bainite fraction decreased markedly from 79 % to 27 %, whereas the ferrite fraction increased. The prior austenite grain size of the bainite was significantly refined, whereas the ferrite grain size remained nearly unchanged. This microstructural evolution led to a gradual reduction in yield strength (YS) at both room and elevated temperatures, decreasing the YS ratio (600 °C/RT) from 0.717 to 0.501. Meanwhile, the Charpy impact energy increased from 32.9 to 169.5 J, thereby demonstrating a clear trade-off between strength and toughness. Notably, the bainite fraction exhibited a strong linear correlation with the strength and YS ratio, whereas ferrite played a dominant role in enhancing toughness, with a complementary contribution from bainitic grain refinement. These findings demonstrate that the mechanical performance of fire-resistant steels can be effectively tuned through process optimization alone, thereby providing a practical strategy for designing steels with balanced strength and toughness.

## 1. Introduction

With the increasing construction of high-rise buildings and rising frequency of fire-related disasters, ensuring the structural integrity of steel under elevated temperatures has become a critical engineering challenge. Although steel is widely used for its high strength and design flexibility, its mechanical properties – especially yield strength (YS) – deteriorate significantly at elevated temperatures, making it vulnerable to fire-induced failures. To overcome this limitation, fire-resistant steels with improved high-temperature strengths have been developed [1–5]. Fire-resistant steels are designed to retain a high YS at 600 °C compared to that at room temperature (RT), and this performance is commonly quantified using the YS ratio (600 °C/RT). A value exceeding 2:3 (≈ 0.67) is generally accepted as the threshold for fire resistance [1], which is significantly higher than the 0.33–0.5 range of conventional carbon steels [4–9].

High-temperature (HT) YS is attributed to the presence of thermally stable microstructures with a high dislocation density, such as bainite, as well as the retardation of dislocation annihilation through mechanisms including solid solution hardening and precipitation hardening [3,5–8,10]. Mo is usually considered the most effective element for improving the HT strength [3,8,9,11]. Wan et al. demonstrated that the solid solution strengthening by Mo is the dominant mechanism at HT, while Mo-induced bainite formation also contributes significantly to HT strength [9,11]. In addition to Mo, Nb is widely known as an element for improving the HT strength in low-alloy steel [3,5–8,12]. Jo et al.

* Corresponding author.
*E-mail address:* lee1626@kims.re.kr (C.-H. Lee).

https://doi.org/10.1016/j.jmrt.2025.07.034
Received 20 May 2025; Received in revised form 25 June 2025; Accepted 5 July 2025
Available online 9 July 2025

reported that the HT strength of fire-resistant steel is enhanced by the precipitation of fine Nb-rich MX particles and the formation of a solid solution of Nb with Mo, both of which hinder dislocation movement and thereby reduce dislocation annihilation [8]. Recent studies have demonstrated that combined microalloying with Nb, Ti, and Mo promotes bainite formation and precipitation hardening, thereby enhancing thermal stability at elevated temperatures [13–15]. Yoshida et al. demonstrated that solute Nb and Nb–C(N) clusters suppressed dislocation motion [7]. However, most studies on fire-resistant steels have focused on alloy design through microalloying with Mo, whereas the influence of thermomechanical processing has received relatively little attention. Furthermore, although strength retention and thermal stability are essential for fire-resistant steels, sufficient toughness is also a critical prerequisite to ensure overall mechanical reliability under service conditions. Nevertheless, a significant gap remains in understanding toughness-related behaviors, as previous research has predominantly focused on fire-resistant properties.

In general, it is widely known that the most effective way to simultaneously enhance both strength and toughness in steel is through grain refinement. From a processing perspective, thermomechanical controlled processing (TMCP) provides a particularly efficient and economical approach to achieve grain refinement in high-strength low-alloy (HSLA) steels [16–19]. Recent process-based studies have also demonstrated that optimizing rolling and cooling strategies – without modifying alloy composition – can effectively tailor the microstructure and enhance fire resistance in structural steels, further supporting the potential of TMCP-like approaches for fire-resistant steel design [20]. In this context, the non-recrystallization temperature ($T_{nr}$) is defined as the temperature below which static recrystallization is suppressed during the interpass interval or subsequent cooling. Deformation induced by rolling below the $T_{nr}$, where recrystallization is inhibited, increases the number of nucleation sites at austenite grain boundaries, thereby promoting grain refinement during the $\gamma$ to $\alpha$ transformation [17,18]. Furthermore, it has been reported that, in fire-resistant steel, the ferrite grain size has a limited effect on the HT strength [9,11]. This suggests that grain refinement may primarily contribute to toughness improvement while maintaining the HT performance. Meanwhile, Cong et al. reported that in the bainite-ferrite microstructure, hot rolling below $T_{nr}$ increased the ferrite fraction, leading to a simultaneous reduction in YS at RT and HT [21]. However, the impact of such microstructural changes on toughness has not been addressed, leaving a critical gap in our understanding of the overall mechanical performance.

In this study, a systematic investigation was performed to clarify the effects of TMCP on grain refinement, phase fraction evolution (bainite vs. ferrite), and their combined influence on both fire-resistant properties and toughness. For the purpose, the alloy composition was fixed using the ingot cutting method, and each cut ingot was hot-rolled to achieve varying TMCP degrees. Subsequently, the microstructures, including the phase fractions, were analyzed and correlated with the mechanical properties, including the YS at RT and HT and the fracture toughness. Interestingly, the results demonstrated that the fractions of bainite and ferrite gradually changed with the TMCP degree. The fire-resistant properties and fracture toughness exhibited contrasting trends. These findings suggest that, even with the same alloy composition, the mechanical properties can be effectively tuned by controlling the TMCP degree. In particular, this study aims to provide a fundamental insight into understanding and optimizing the balance between fire resistance and toughness in microalloyed steels through controlled thermomechanical processing. Moreover, the observed trade-off between fire resistance and toughness highlights the necessity of process-based strategies that simultaneously address both requirements for structural reliability.

## 2. Experimental method

### 2.1. Material preparation

In this study, to investigate the effect of TMCP on the mechanical properties, a single 100 kg ingot with a chemical composition of Fe-0.11C-0.31Si-1.59Mn-0.32Cr-0.28Mo-0.05Nb (wt.%) was fabricated using vacuum induction melting (VIM). The VIM ingot was first divided into two halves, each of which was austenitized at 1200 °C for 2 h and hot-rolled from an initial thickness of 155 mm–100 mm, followed by air cooling. Each rolled half was then further sectioned, and five of the resulting sections were selected for additional thermomechanical processing. These five samples were austenitized at 1200 °C for 2 h and subsequently subjected to seven-pass hot rolling to a final thickness of 15 mm. The average thickness reduction per pass was approximately 25 %, with comparable reductions applied above and below the $T_{nr}$ temperature. The austenitizing temperature was chosen based on the alloy composition and further validated by thermodynamic calculations using Thermo-Calc. software (TCFE12 database), which predicted that NbC would fully dissolve above approximately 1140 °C in this steel (Supplementary Fig. S1). Specifically, among the seven passes, the ratios of rolling conducted above and below $T_{nr}$ were controlled at 7:0 (no TMCP), 6:1, 5:2, 4:3, and 1:6. The $T_{nr}$ temperature for a given alloy composition was calculated using a well-established equation, as follows [18,19]:

$$T_{nr} = 887 + 464C + \left[6445Nb - 644(Nb)^{1/2}\right] + \left[732V - 230(V)^{1/2}\right] + 890Ti + 363Al - 357Si \quad (1)$$

where all the alloying elements are expressed in wt.%. By considering the addition of 0.005 wt% Al as a deoxidizer, $T_{nr}$ was calculated to be approximately 1007.43 °C. Based on this, hot rolling above $T_{nr}$ was completed, followed by air cooling to approximately 930 °C before initiating the rolling below $T_{nr}$, as schematically illustrated in Fig. 1. After the final rolling pass, all specimens were air-cooled to RT. For convenience, the specimens processed with rolling pass ratios (above: below $T_{nr}$) of 7:0, 6:1, 5:2, 4:3, and 1:6 were designated as TM70, TM61, TM52, TM43, and TM16, respectively. In addition, the TMCP degree is defined as the fraction of rolling passes conducted below the $T_{nr}$ out of the total number of rolling passes: an increase in TMCP degree therefore indicates a greater portion of deformation occurring in the $T_{nr}$ region, resulting in more severe thermomechanical conditions during the final stage of processing.

### 2.2. Microstructural characterization

The overall microstructural evolution with respect to the TMCP degree was examined by optical microscopy (OM). In addition, more detailed microstructural analysis was conducted using field-emission

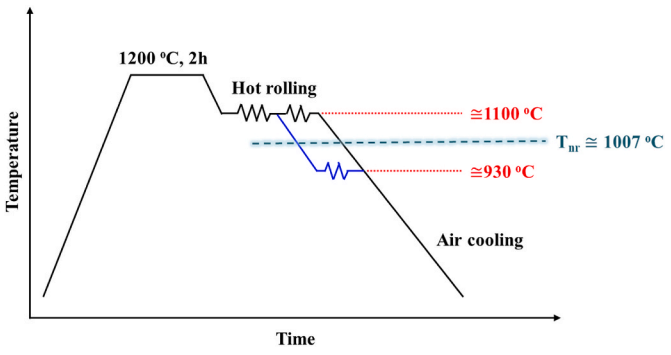


**Fig. 1.** Schematic of the TMCP schedule used for sample preparation.

scanning electron microscopy (FE-SEM), electron backscatter diffraction (EBSD), and transmission electron microscopy (TEM) for phase identification. For the OM and SEM observations, the specimens were polished and etched using a nital solution composed of 3 mL of nitric acid and 97 mL of ethanol, whereas the EBSD specimens were finalized with a colloidal silica suspension. For TEM analysis, thin foil specimens were prepared by twin-jet electrolytic polishing in a solution containing 10 % perchloric acid and 90 % methanol at – 30 °C. Additionally, atomic probe tomography (APT) was performed to analyze the solid solution, clustering, and precipitation in the matrix. For this, tip-shaped specimens were prepared using focused ion beam (FIB) milling and maintained in a vacuum chamber of $1.0 \times 10^{-11}$ Torr at −233.15 °C. Field evaporation was carried out using a UV pulse laser ($\lambda = 355$ nm) with a power of 100 pJ and a frequency of 200 kHz at an evaporation rate of 1.5 %. After acquisition, the data were analyzed using Interactive Visualization and Analysis Software (IVAS, AP Suite 6.1).

### 2.3. Mechanical testing method

The RT tensile tests were performed using plate-type sub-sized specimens prepared in accordance with the ASTM E8M standard. The tests were conducted on an INSTRON 4485 universal testing machine at a constant crosshead speed of 2 mm/min. For HT tensile testing, small round specimens were used, conforming to the ASTM E8M standard. Testing was performed at 600 °C after a 20 min holding time at the target temperature. The crosshead speed was set to 0.2 mm/min prior to yielding and 1.5 mm/min after yielding. All HT tests were conducted using a SHIMADZU AG-250KNXPLUS machine in accordance with the ASTM A370-22 standard. To evaluate the fracture toughness, V-notched specimens with dimensions of 55 (L) × 10 (W) × 10 (t) $mm^3$ were prepared, and Charpy impact tests were conducted at – 5 °C using a Charpy impact machine (IT406, TINIUS OLSEN). To ensure reliability, the RT tensile and Charpy impact tests were performed three times, whereas the HT tensile tests were conducted twice. The average values were used for the analysis.

## 3. Results

### 3.1. Microstructural evolution with varying TMCP degrees

The OM micrographs in Fig. 2(a1-e1) show the overall microstructural evolution in TM70, TM61, TM52, TM43, and TM16. The grain shape becomes gradually elongated, and the rolled strips observed in the etched microstructure, which align along the rolling direction, become increasingly prominent from TM70 to TM16. In addition, a dual-phase microstructure appears in TM52, TM43, and TM16, with more fraction of the secondary phase. The corresponding representative microstructures at higher magnifications are shown in Fig. 2(a2-e2). Both TM70 and TM61 consist of fully bainitic microstructures, without noticeable difference between them. However, starting from TM52, ferrite or ferrite-pearlite regions are clearly observed, and their fractions increase with an increase in TMCP degree. In addition, the bainite grain size tends to decrease as the ferrite-pearlite grains begin to form, particularly in TM52. Moreover, the ferrite grains appear to become progressively finer from TM52 to TM16. Fig. 3 shows the variation in the phase-specific average grain sizes of bainite and ferrite with the TMCP degree. The prior austenite grain size (PAGS) of bainite is significantly reduced from 33.91 μm to 18.14 μm when more rolling passes were conducted below the $T_{nr}$. On the other hand, although the grain size of ferrite also slightly decreases, the reduction is relatively minor, from 7.43 μm to 6.75 μm. Such changes in the phase fractions of bainite and ferrite, along with grain refinement, are considered to influence the mechanical properties, particularly the strength and fracture toughness.

To analyze the characteristic features of each microstructure, two representative specimens, TM70 and TM16, were selected as extreme cases corresponding to the lowest and highest TMCP degrees, respectively. Fig. 4(a–c) and **4(d–f)** present the FE-SEM and TEM micrographs of TM70 and TM16, respectively. In Fig. 4(a), the microstructure of TM70 appears to be fully bainitic, in which prior austenite grain boundaries (PAGBs) are clearly observed, as indicated by white dashed lines. As shown in Fig. 4(b), the overall matrix of TM70 consists of bainitic ferrite; however, due to continuous cooling, it contains a mixture of multiple phases, resulting in a more complex microstructure

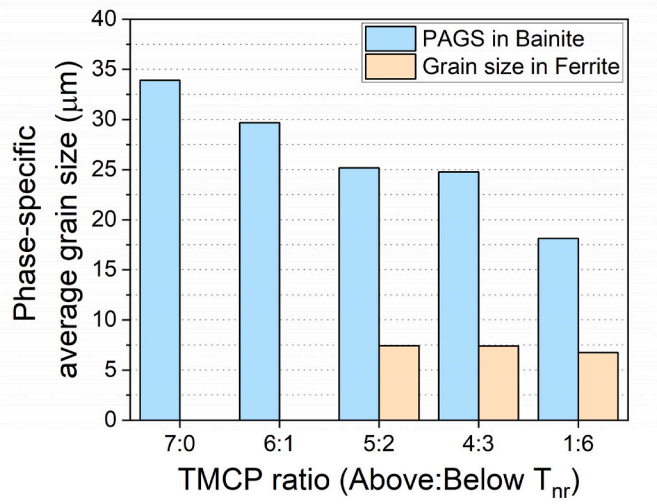


**Fig. 3.** Phase-specific average grain size of bainite and ferrite across different TMCP ratios (Above:Below $T_{nr}$).

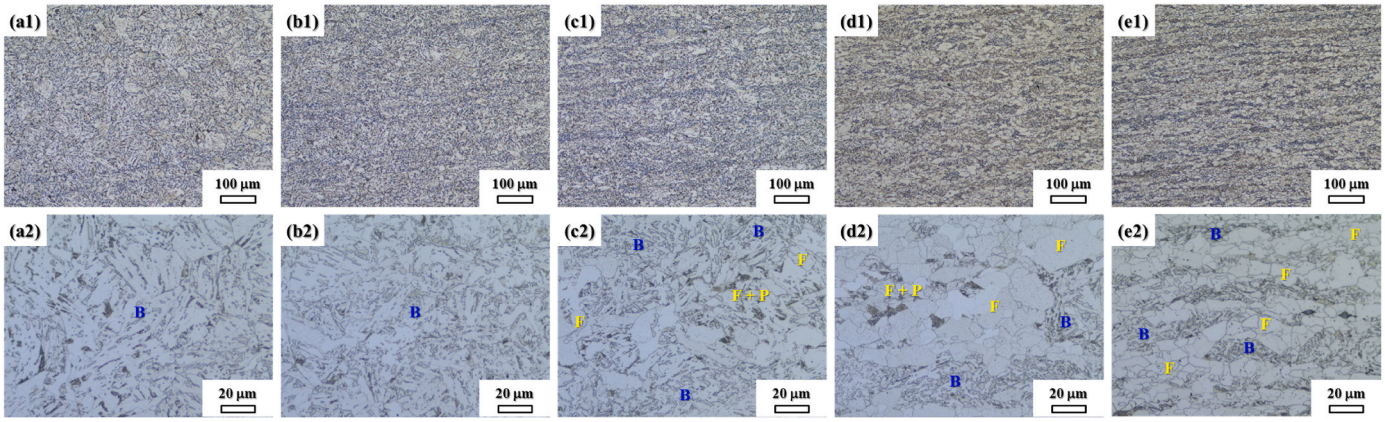


**Fig. 2.** OM micrographs of the microstructures of TMCP-processed steels: (a1, a2) TM70, (b1, b2) TM61, (c1, c2) TM52, (d1, d2) TM43, and TM16.

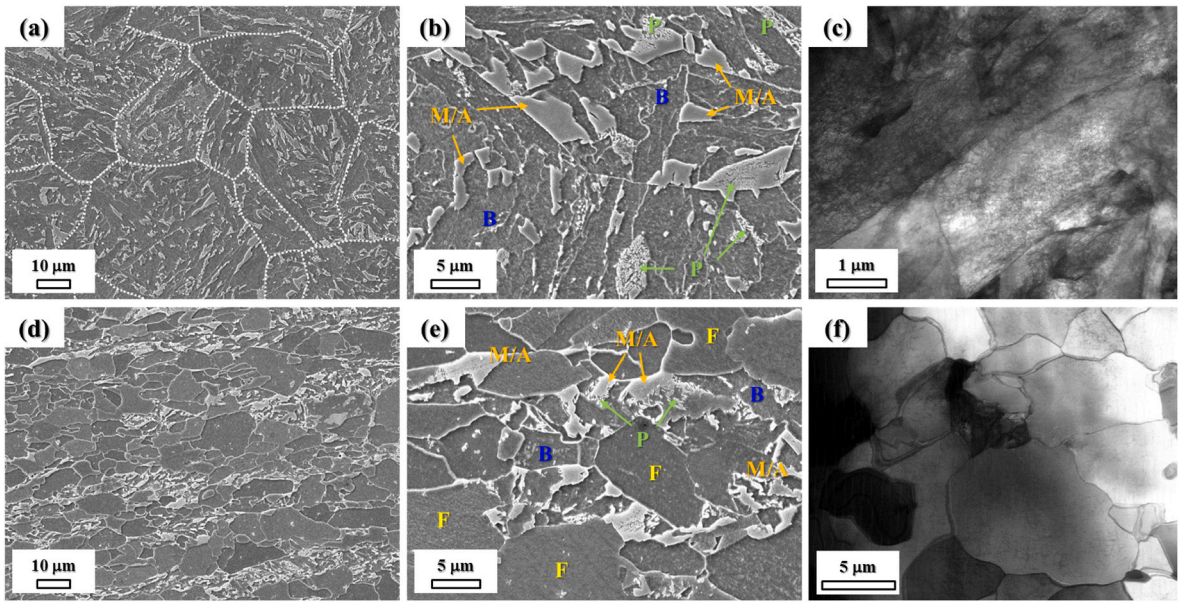


**Fig. 4.** Comparison of the microstructures between TM70 and TM16 steels using FE-SEM and TEM microscopy: (a–c) TM70 and (d–f) TM16 steel.

than that of conventional bainite. The phases may include carbide-free bainite (B), martensite-austenite (M/A) constituents in the form of flakes, and degenerated pearlite (P). For TM16, as shown in Fig. 4(d), a high fraction of ferrite is observed, which is predominantly aligned along the deformation rolled strips. In addition, the regions between these ferrite bands consist of a complex mixture of phases, including slightly deformed polygonal ferrite, martensite-austenite (M/A) constituents, degenerated pearlite, and granular bainite, as shown in Fig. 4

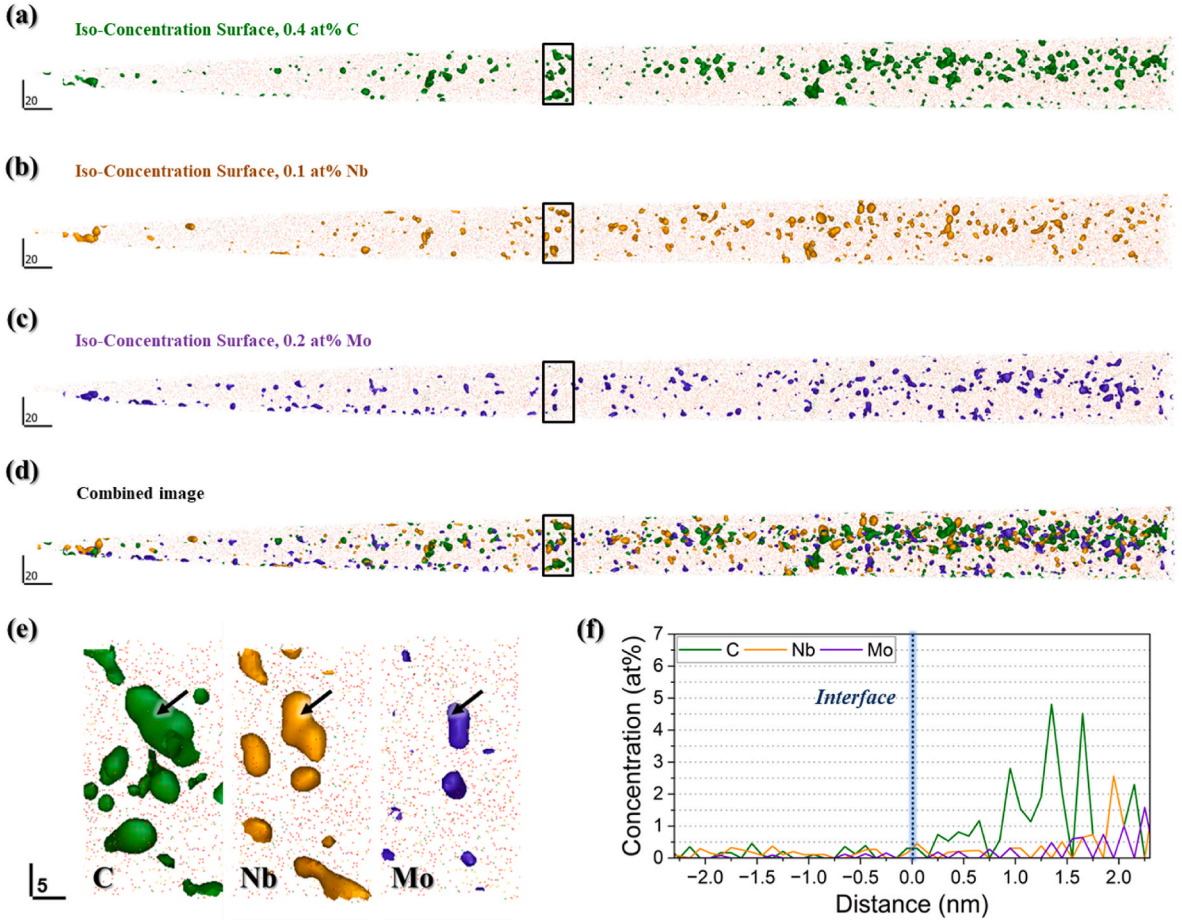


**Fig. 5.** APT analysis of TM70 steel: iso-concentration surfaces of (a) 0.4 at% C, (b) 0.1 at% Nb, (c) 0.2 at% Mo, and their combined distribution; (e) a magnified view of a fine Nb-rich precipitates extracted from the black boxes in (a–d); and (f) a line concentration profile along the black arrows in (e).

(e). The dominant phases in the TM70 and TM16 matrices (bainite and ferrite) are clearly identified in the TEM images shown in Fig. 4(c) and (f), respectively. The bainite phase exhibits a carbide-free lath morphology with a high dislocation density, whereas the ferrite appears to be recrystallized, as indicated by its polygonal shape and very low dislocation density.

Although no precipitates are observed in any of the specimens during the TEM analysis, APT analysis was performed on the TM70 specimen to further investigate the elemental distribution of Nb atoms. Fig. 5(a–d) show the iso-concentration surface images of 0.6 % C, 0.1 % Nb, and 0.3 % Mo, and their combined distributions, respectively. Fine Nb-rich particles, typically smaller than 10 nm, are identified for 0.1 % Nb. The colocalization of C and Nb suggests that these particles are NbC precipitates or Nb–C clusters. A representative example is magnified in Fig. 5(e), where Nb and C coexist and Mo is also present near the particle, which is likely segregated at the interface. Fig. 5(f) shows the line concentration profile along the black arrows in Fig. 5(e), revealing weak but distinct peaks of Nb and Mo, in addition to a C peak, which supports the presence of (Nb,Mo)C-type precipitates. However, a significant portion of the Nb remains in the solid solution, indicating that most of the Nb has not precipitated. This likely explains the absence of clear NbC precipitates in the TEM images, not only in TM70 but also in the other specimens. Consequently, the majority of the Nb is present either as a solid solution or in the form of fine clusters, with only a limited fraction precipitating as extremely fine NbC.

### 3.2. Mechanical properties across different TMCP ratios

Fig. 6(a) and (b) present the variations in yield and tensile strength at RT and 600 °C, respectively, across different TMCP ratios. In Fig. 6(a), the RT tensile strength remains relatively constant at approximately 700 MPa, even with an increasing number of rolling passes conducted below $T_{nr}$, whereas the YS gradually decreases from 508 to 453 MPa. In contrast, at 600 °C, both strengths exhibit a decreasing trend, as shown in Fig. 6(b). Interestingly, the reduction in YS at 600 °C becomes more pronounced with a greater number of rolling passes conducted below $T_{nr}$. While TM70 and TM61 exhibit a relatively modest decrease in YS compared to RT (on average, from 501 to 362 MPa), the reduction is more pronounced with the increased TMCP degree, reaching nearly 50 % in TM16 (from 453 to 227 MPa). Given the nearly constant tensile strength at RT, the extent of the reduction at 600 °C increased with the increased TMCP degree, consistent with the YS trend. The strength reduction is likely associated with the microstructural features, specifically the variations in the fractions of bainite and ferrite, and the changes in grain size induced by TMCP.

Fig. 7 shows the YS ratio (600 °C/RT) and the impact energy across different TMCP ratios. Notably, with the increasing number of rolling passes conducted below the $T_{nr}$, the YS ratio gradually declines, while

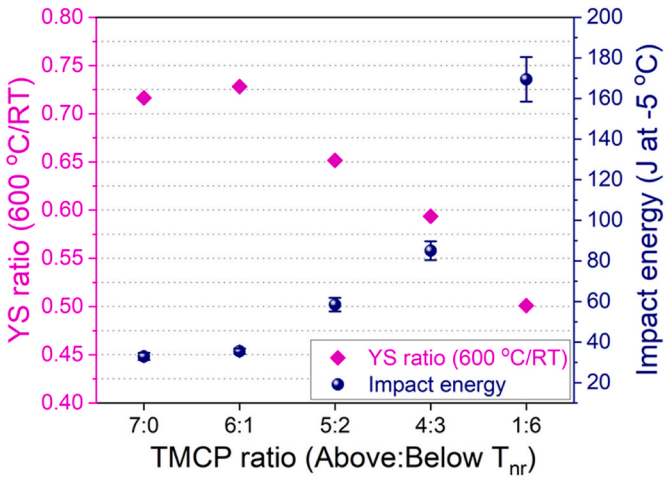


**Fig. 7.** Change in YS ratio (600 °C/RT) and impact energy across different TMCP ratios (Above:Below $T_{nr}$).

the impact energy exhibits a pronounced increase, showing a clear trade-off trend. Specifically, the mechanical properties are maintained in TM70 and TM61, where the average YS ratio and impact energy are 0.722 and 34.2 J, respectively. Although the toughness is still limited at this stage, the YS ratio exceeds 2/3, indicating excellent fire resistance. However, beyond this point, the YS ratio declines sharply from 0.728 in TM61 to 0.501 in TM16, while the impact energy markedly increases from 35.5 J in TM61 to 169.5 J (TM16). This trend is consistent with the increase in ductility, particularly elongation, with an increasing TMCP degree (Supplementary Fig. S2), which may have partially contributed to the enhanced fracture toughness. This inverse relationship highlights the competing effects of TMCP on the strength retention and toughness of fire-resistant steel. While it is evident that TMCP influences both the phase fraction and grain size, it remains unclear which factors dominate the observed tradeoff between strength and toughness. To address this, a detailed analysis was conducted to quantify the evolution of the ferrite and bainite fractions and grain refinement under varying TMCP conditions.

## 4. Discussion

### 4.1. EBSD-based quantification of bainite and ferrite phases

To understand the microstructural basis of the strength-toughness trade-off observed in Section 3.2, EBSD analysis was conducted to quantify the evolution of ferrite under varying TMCP conditions. Fig. 8 shows the EBSD results of TM70 **(a1-a3)**, TM61**(b1-b3)**, TM52**(c1-c3)**,

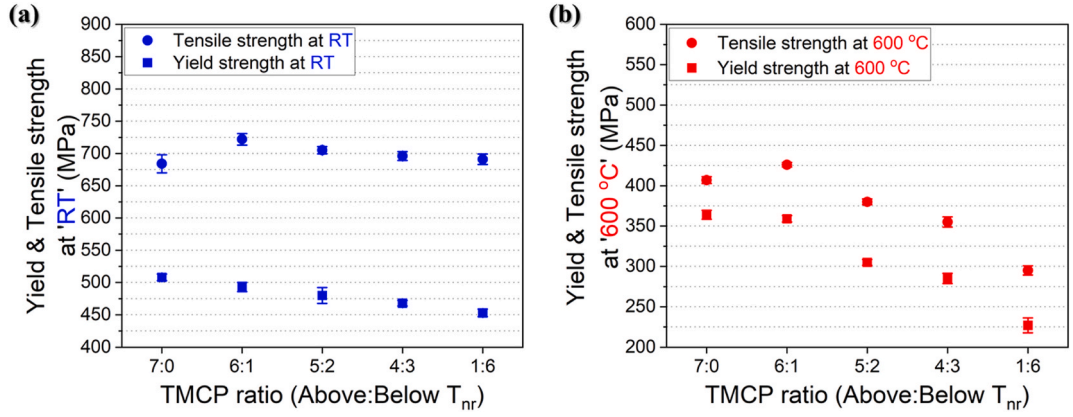


**Fig. 6.** Change in yield and tensile strength at (a) RT and (b) 600 °C across different TMCP ratios (Above:Below $T_{nr}$).

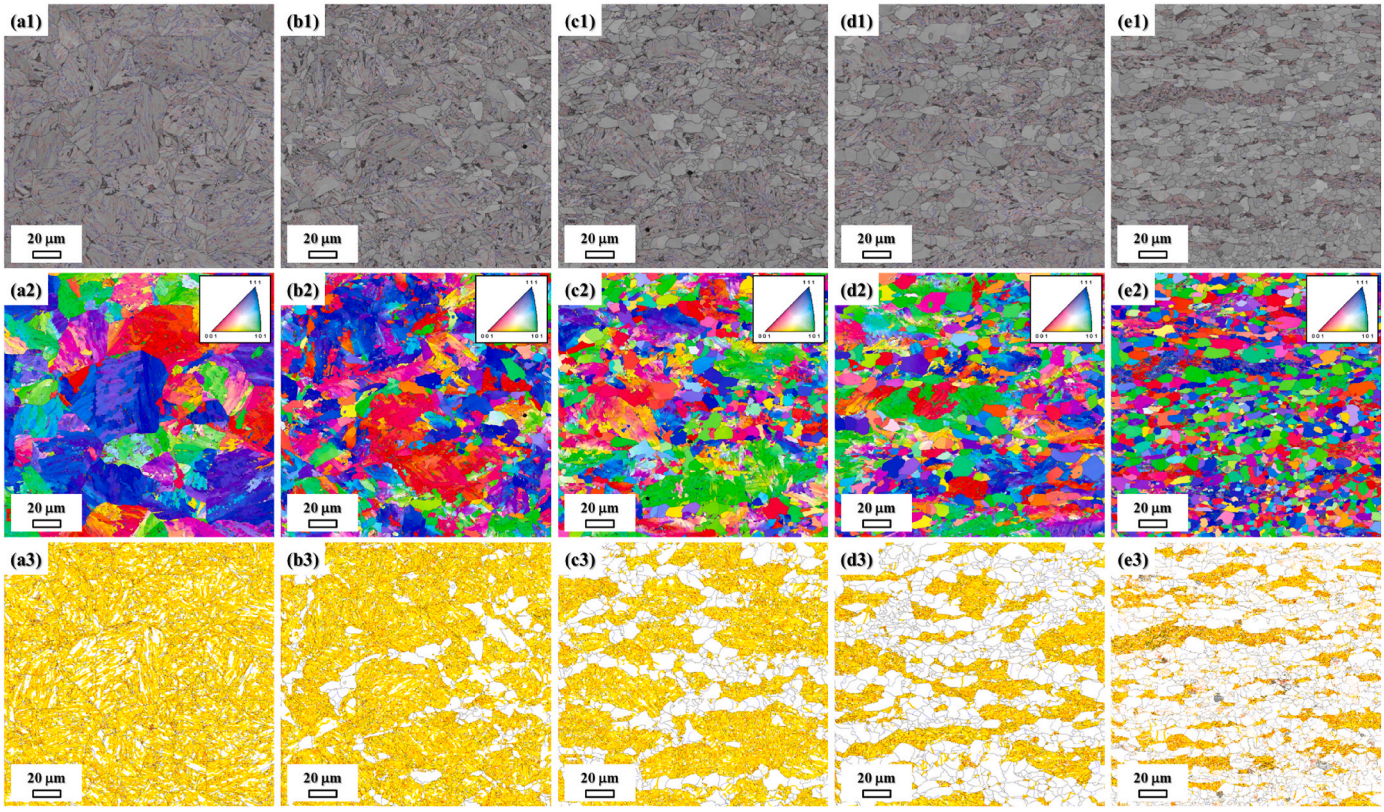


**Fig. 8.** EBSD analysis of TMCP-processed steels: (a1-e1) IQ maps, (a2-e2) IPF-Z maps, and (a3-e3) KAM maps with threshold values of each specimen: (a1-3) TM70, (b1-3) TM61, (c1-3) TM52, (d1-3) TM43, and (e1-3) TM16.

TM43**(d1-d3)**, and TM16**(e1-e3).** The microstructural information is shown in three forms: (1) image quality (IQ) maps in Fig. 8(a1-e1), which provide insight into the overall microstructure and defect density; (2) inverse pole figure (IPF) maps along the rolling direction in Fig. 8(a2-e2), illustrating the crystallographic orientation of grains; and (3) kernel average misorientation (KAM) maps in Fig. 8(a3-e3), highlighting the local lattice strain and misorientation within grains. In Fig. 8(a1-a3), TM70 consists of a fully bainitic structure with a well-preserved lath morphology. Although TM61 steel appears to be fully bainitic in the OM observations (Fig. 2), EBSD analysis reveals traces of ferrite, as shown in Fig. 8(b1-b3), likely owing to its higher resolution and strain sensitivity, which allow the detection of fine ferrite that may not have been clearly distinguishable by OM. From TM52 onward, a significant fraction of ferrite is observed, which continues to increase with increasing TMCP degree up to TM16. At the same time, the grains become more refined and progressively elongated, particularly in the ferrite phase, which is consistent with the increasing ferrite fraction.

The full bainitic microstructure in TM70 is attributed to the high hardenability of the alloy system in combination with the relatively fast cooling rate of the austenite phase. In particular, Mo (0.28 wt%), Mn (1.59 wt%), and Cr (0.32 wt%) are known to enhance hardenability by suppressing the formation of ferrite and pearlite. Among them, Mo plays a particularly critical role. Although it slightly retards the generation of bainite, its stronger effect in suppressing ferrite and pearlite promotes bainite formation under continuous cooling [6,9,18,22]. In addition, Mo increases the solubility of Nb in austenite, delaying Nb-rich precipitation until the ferrite transformation stage and resulting in finer particles [5,18,22]. These fine particles are often beyond the resolution of TEM; however, their presence has been confirmed as nanoscale precipitates or clusters by APT analyses. Nb also enhances the hardenability by retarding static recrystallization and slowing ferrite growth via solute drag [18]. Consequently, Nb and Mo act synergistically to stabilize bainite formation by suppressing austenite decomposition during air cooling. Meanwhile, the ferrite fraction increased when more rolling passes were conducted below the $T_{nr}$. This phenomenon is attributed to the suppression of static recrystallization and the accumulation of strain in austenite below $T_{nr}$. The retained strain energy promotes the formation of deformation bands and elongated austenite grains, which in turn provide favorable nucleation sites for the $\gamma$ to $\alpha$ transformation during subsequent cooling [17,18]. Thus, as the TMCP degree increases, the grains become increasingly elongated, and the ferrite and bainite phases tend to form a banded structure aligned with the rolling direction, as shown in Fig. 8(a1-e1) and **8(a2-e2)**. Consequently, the ferrite fraction is increased, particularly in steel subjected to more rolling passes below $T_{nr}$.

A reliable method for distinguishing between bainite and ferrite is required to quantitatively evaluate the phase evolution induced by TMCP. Because the fractions of these phases are closely related to their mechanical properties, particularly their strength and toughness, accurate phase quantification is essential for elucidating their contributions. Although the EBSD maps clearly reveal qualitative differences in the microstructure, accurate phase quantification requires consistent and objective classification criteria. Among the various EBSD-derived parameters, KAM has been reported to be more sensitive and reliable than others, such as IQ or grain orientation spread (GOS), particularly for distinguishing bainitic structures from recrystallized ferrite. Zaefferer et al. introduced the concept of a maximum KAM threshold value ($KAM_{max}$), which was defined as the inflection point of the KAM histogram. The proposed $KAM_{max} = 0.6 \pm 0.05^{o}$ showed the highest agreement with manual phase segmentation in low-alloyed Al-TRIP steels [23]. In their classification, bcc-indexed pixels with $KAM < KAM_{max}$ were categorized as ferrite, while those with $KAM \geq KAM_{max}$ were considered bainite, reflecting the degree of internal misorientation in each phase. Furthermore, recent studies adopted KAM-based thresholds to define the phase boundaries in ferrite-bainite microstructures. For example, Jentner et al. applied a KAM-based EBSD approach to

distinguish polygonal ferrite from bainitic regions in HSLA steels [24], and Kang et al. used a threshold of 0.5° in their analysis of quenching and partitioning steels [25]. Based on these insights, this study conservatively adopted 0.7° as the $KAM_{max}$ value to distinguish ferrite ($KAM < KAM_{max}$) from low-temperature transformation products such as bainite ($KAM \geq KAM_{max}$). While KAM values in the range of 0.7° – 1.2° may include the contributions from deformed ferrite, transitional structures, or overlapping regions – all regions with KAM ≥ 0.7° are designated as "bainite" for practical quantification, in line with previous EBSD-based classification.

The KAM maps shown in Fig. 8(a3-e3) were generated based on a threshold value of 0.7°, as previously described, to visually distinguish bainite from ferrite. Using this classification criterion, the phase fractions of each specimen were quantitatively measured. Fig. 9 presents the changes in the fractions of bainite and ferrite across different TMCP degrees. For TM70, the bainite fraction was estimated to be 79.3 %, with only a slight decrease to 73.8 % in TM61. However, marked reductions were observed from TM52 onward (57.2 % for TM52, 36.5 % for TM43, and 27.0 % for TM16), indicating a threshold-like transition in phase evolution. This abrupt shift in the phase fraction is strongly aligned with the mechanical property trends shown in Figs. 6 and 7, where both YS and toughness remain relatively stable up to TM61, but change significantly from TM52 onward [26]. A comparable correlation between phase morphology and mechanical behavior was demonstrated by Chen et al. [27], who employed EBSD-based quantification of austenite and ferrite to explain the strength-ductility synergy in medium-Mn steels. Although their alloy system and transformation mechanisms differ from those in this study, their emphasize on phase fraction control as a predictor of mechanical performance aligns well with the present approach. The strong correlation between the bainite fraction and key mechanical properties will be further examined in Section 4.2. In addition, the measured bainite fraction was reasonably fitted by a second-order polynomial regression with respect to the number of rolling passes below $T_{nr}$, represented by the equation $y = 0.0064x^2 - 1.2215x + 83.57$, with a high coefficient of determination ($R^2 = 0.9454$), implying the potential for the approximate prediction of the phase balance based on TMCP conditions.

### 4.2. *Reinterpreting the correlation between phase fraction and mechanical properties*

Although Section 4.1 demonstrated the systematic evolution of the bainite and ferrite fractions under varying TMCP conditions, a more fundamental question arises: To what extent do these microstructural changes quantitatively influence the mechanical performance of steel? In this section, we reinterpret the relationship between the TMCP conditions and mechanical properties through the lens of phase fraction evolution. By correlating the quantified bainite fraction with the YS, toughness, and fire-resistance performance, we aimed to identify the microstructural factors that govern the mechanical behavior.

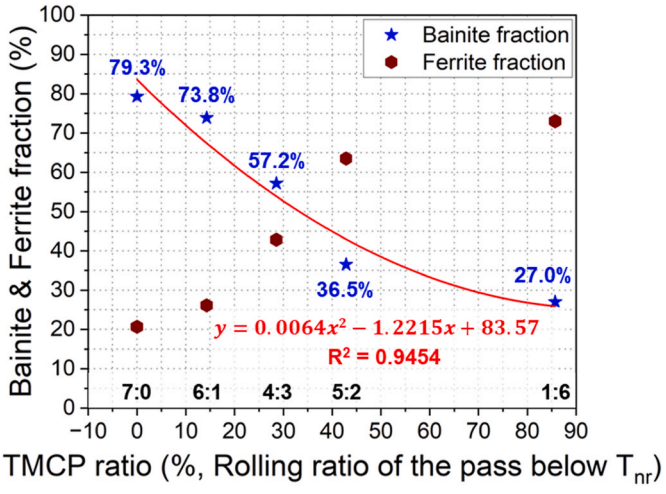


**Fig. 9.** Changes in the fractions of bainite and ferrite with increasing proportion of rolling passes below the $T_{nr}$ temperature.

Fig. 10(a) and (b) show the YS at RT and 600 °C as a function of bainite fraction, respectively. Interestingly, both YSs exhibit a strong linear correlation with the bainite fraction, underscoring the critical role of phase composition. At RT, the YS increased linearly with the bainite fraction, following the regression equation $y = 0.9171x + 430.18$, with a $R^2$ of 0.9564. Similarly, at 600 °C, the relationship was also linear, as described by $y = 2.4130x + 175.86$ ($R^2 = 0.9416$). The high $R^2$ values demonstrate that bainite fraction is the dominant factor in strength development at both temperatures.

Fig. 11(a) and (b) present the YS ratio and impact energy as a function of bainite fraction, respectively. These two properties are directly related to the fire-resistant and damage-tolerant behaviors of steel, making them critical indicators of structural performance under high-temperature conditions. A closer examination reveals contrasting trends between the YS ratio and impact energy, confirming that the strength-toughness trade-off is governed by phase evolution. The YS ratio (600 °C/RT), as inferred from the individual YS trends shown in Fig. 10, also exhibits a linear relationship with the bainite fraction ($y = 0.0038x + 0.4277$, $R^2 = 0.9035$). Although the $R^2$ value of YS ratio was slightly lower than that obtained for individual YS, it remained above 0.90, indicating a reasonably strong and reliable correlation with bainite fraction. In contrast, fracture toughness demonstrates a nonlinear relationship with bainite fraction. It decreased from 169.5 J (TM16) to 32.9 J (TM70) and following a second-order polynomial regression described by $y = 0.0065x^2 - 9.1389x + 355.82$ ($R^2 = 0.9257$). This contrast implies that while the bainite fraction is a dominant factor for the strength and YS ratio, the fracture toughness is likely influenced by additional microstructural parameters beyond the phase fraction. Nevertheless, a clear trade-off emerges between the YS ratio and fracture toughness, highlighting the opposing effects of phase evolution on strength and toughness.

In this study, because the alloy composition was constant and the detailed distribution of the precipitates could not be characterized, the contributions of solid solution and precipitation strengthening were assumed to be equivalent for bainite and ferrite. Furthermore, with varying TMCP degrees, the grain size of ferrite decreased slightly from 7.43 to 6.75 μm, as shown in Fig. 3. For bainite, the effective grain size exhibited a narrow variation between 1.15 and 1.78 μm, as quantified based on the low-angle grain boundaries (LAGBs) within the 2–7° range through EBSD analysis [28,29] (Supplementary Fig. S3). Considering that the maximum grain size variation within each phase was less than 0.7 μm, the contribution of grain refinement to YS was minor. Therefore, the phase fraction is inferred to be the dominant microstructural factor governing the strength evolution under different TMCP conditions.

Although Nb microalloying is typically associated with precipitation strengthening, no distinct NbC precipitates were observed in the TEM analysis across all TMCP specimens. This may be attributed to the extremely fine size or clustering nature of Nb-rich features, making them difficult to resolve using conventional TEM. To overcome this limitation, APT was performed on TM70, which revealed nanoscale (Nb,Mo)C precipitates and Nb–C clusters smaller than 10 nm (Fig. 5). Based on these findings, a phase fraction-based rule-of-mixture model was employed to estimate strength contribution, implicitly capturing the effects of undetectable fine precipitates and solute atoms within each phase.

Building on the basis, the evolution of YS during TMCP was closely correlated with the bainite and ferrite fractions. To explain this relationship, a simple linear rule-of-mixture model was employed, which is a widely accepted first-order approximation in dual-phase steel studies,

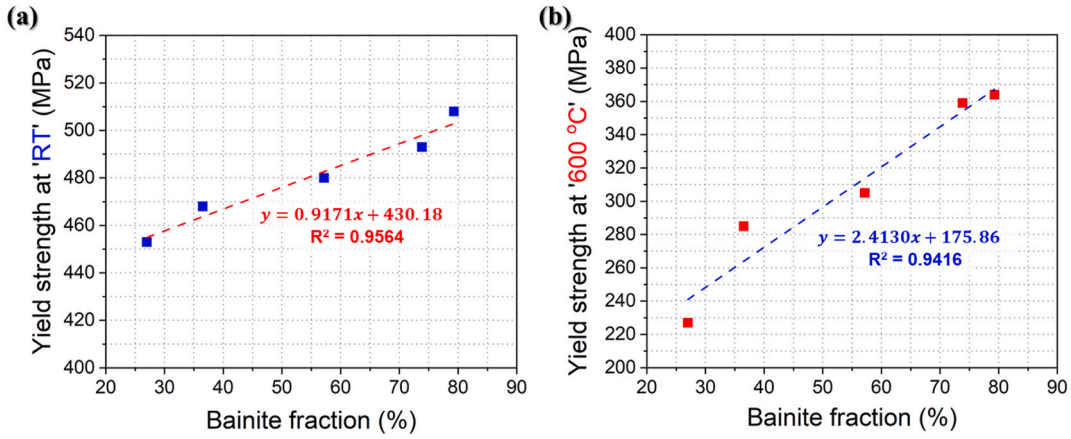


**Fig. 10.** Change in yield strength at (a) RT and (b) 600 °C as a function of bainite fraction.

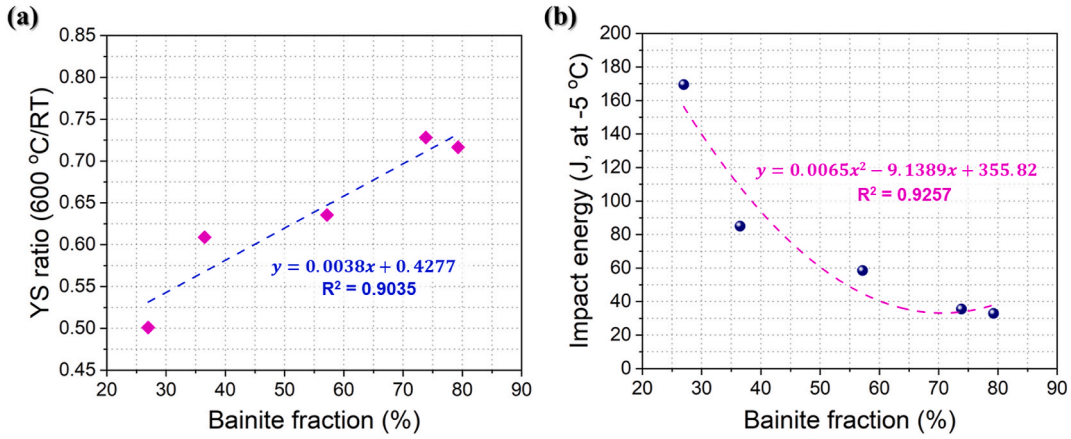


**Fig. 11.** Change in (a) YS ratio (600 °C/RT) and (b) Impact energy as a function of bainite fraction.

particularly for ferrite-martensite systems [30,31]. Although these models do not consider the complex interactions between phases, they are effective when the phase morphology is relatively uniform and the phase fraction is the dominant factor. Given the analogous dual-phase nature of ferrite-bainite microstructures, this approach can provide fundamental insights into the mechanical behavior. In this model, the overall YS at a given temperature is expressed as

$$\sigma_y = f_B \cdot \sigma_B + (1 - f_B) \cdot \sigma_F \tag{3}$$

where $\sigma_y$ is the measured YS, $f_B$ is the bainite fraction, and $\sigma_B$ and $\sigma_F$ are the intrinsic YSs of bainite and ferrite, respectively. Using the measured YSs and phase fractions of TM70 and TM16 as boundary conditions, the intrinsic YS values at RT were estimated to be approximately 530 and 425 MPa for bainite and ferrite, respectively, while those at 600 °C were 415 and 157 MPa, respectively. Although dual-phase steels often exhibit complex strengthening interactions, this simplified model provides a reasonable approximation by capturing the combined effects of grain refinement, dislocation density, solid solution, and precipitation hardening within each phase. Importantly, the analysis reveals that bainite retains its strength more effectively when the temperature increases from RT to 600 °C, with a 22 % YS drop (from 530 to 415 MPa) compared to the 63 % drop in ferrite (from 425 to 157 MPa). This underscores the superior high-temperature stability of bainite and its critical role in fire resistance performance [10]. A similar trend was reported by Sim et al. who demonstrated that bainite-based microstructures retained tensile strength and fatigue resistance more effectively than ferrite-rich counterparts at elevated temperatures, further supporting the advantage of bainitic morphology for fire-resistant structural applications [10]. Although dislocation density was not directly measured, previous work on Nb–Mo fire-resistant steels has shown that these elements suppress dislocation annihilation at elevated temperatures, thereby preserving strength. Jo et al. reported that the reduction in dislocation density at 600 °C was significantly lower (25.3 %) in Nb–Mo steels than in conventional C–Mn steels (41.3 %) [8]. The relatively high YS ratio observed in this study suggests that similar mechanisms may contribute to the retention of high-temperature strength. Further investigation of dislocation substructures would be beneficial to verify this mechanism.

Unlike YS, the fracture toughness followed a nonlinear relationship with the bainite fraction, suggesting the involvement of additional microstructural factors. Polygonal ferrite exhibits equiaxed and recrystallized grain morphology with limited coarse carbides; therefore, it generally offers higher resistance to cleavage fracture than bainite. Therefore, an increase in ferrite fraction seems to be the most critical contributor to toughness enhancement [32]. In addition to the phase fraction, grain size also plays a role. While the ferrite grain size changed only slightly across different TMCP conditions (7.43–6.75 μm), PAGS of bainite exhibited a substantial refinement – from 33.91 μm (TM70) to 18.14 μm (TM16) (Fig. 3). Numerous studies have reported that the fracture toughness in bainitic or martensitic microstructures is more sensitive to PAGS than to internal substructure features, such as lath or block boundaries, which are typically associated with LAGBs [32–34]. This highlights the fundamental distinction between strength, which is governed by dislocation movement, and toughness, which depends on the resistance to crack propagation. To assess the relative contributions of phase fraction and grain refinement, a multiple linear regression

model was developed using the bainite fraction ($f_B$) and PAGS ($d_B$) as independent variables. The resulting equation is as follows:

$$\text{Fracture toughness (J)} = 271.72 - 87.38 \cdot f_B - 5.61 d_B \quad (4)$$

where $d_B$ is the average PAGS (μm). The model shows a high explanatory power ($R^2 = 0.8630$), although the limited sample size (n = 5) imposed statistical constraints on the interpretation of coefficient significance. Moreover, the magnitude of the regression coefficients should not be directly compared because the two variables differ in scale and units. Despite these limitations, the model provides valuable insights into the relative influence of microstructural factors on fracture toughness. The negative coefficients of both $f_B$ and $d_B$ indicate that the increases in bainite fraction and PAGS are associated with a reduction in toughness. Although the numerical coefficient of $f_B$ is larger than that of $d_B$, this does not necessarily reflect their true physical influence because of their different scales and units. Based on the fracture toughness trend and the extent of phase transformation, the decrease in the bainite fraction can be interpreted as the primary microstructural factor governing the toughness improvement. In contrast, PAGS reduction acts as a secondary factor, fine-tuning the microstructure and further enhancing crack resistance. Consequently, our results indicated that the increased ferrite fraction played a dominant role, whereas bainite grain refinement via PAGS reduction provided a complementary contribution to toughness enhancement. The linear correlation is particularly meaningful for fire-resistant steels, where maintaining YS at elevated temperatures is essential. Among typical microstructures, martensite exhibits high strength but poor thermal stability, and ferrite-pearlite offers better stability but limited strength [8,35]. In contrast, bainite retains relatively high strength even at 600 °C due to its high dislocation density and thermal stability. Therefore, the strong linear relationship between bainite fraction and YS (including YS ratio) confirms that increasing bainite content is an effective strategy to simultaneously ensure high strength and fire resistance in low-alloy steels, providing a critical microstructural guideline for TMCP optimization. This trade-off behavior underscores that although intensive TMCP may reduce high-temperature strength, the concurrent improvement in fracture toughness can substantially enhance structural reliability under fire exposure [36]. Thus, the engineering significance of low-temperature rolling in fire-resistant steels lies not only in strength retention, but in achieving a balanced combination of fire resistance and toughness for practical structural applications.

Although the formation of ferrite under low-temperature deformation is a well-known phenomenon in steels, this study focuses on how such microstructural evolution affects the balance between fire-resistance and fracture toughness in fire-resistant steels. By adjusting the TMCP conditions, we show that the ferrite-bainite fraction can be systematically tuned, offering a process-based strategy to achieve improved or balanced performance without compositional changes. These findings clarify the underlying mechanism governing the strength and toughness during the TMCP of fire-resistant steel. The phase fraction evolution and bainitic grain refinement contributed distinctively to both strength and toughness, offering a microstructural explanation for the observed trade-off behavior.

## 5. Conclusion

In this study, we investigated the effect of TMCP on the microstructural evolution and mechanical properties of fire-resistant steel, with a particular focus on the strength-toughness trade-off. To this end, the alloy composition was fixed by sectioning a single ingot, and the degree of TMCP was controlled by systematically varying the ratio of rolling passes conducted above and below $T_{nr}$. This processing route resulted in varying phase fractions and grain sizes, which were characterized using OM, FE-SEM, TEM, and EBSD. To evaluate the fire-resistance performance, tensile tests were conducted at RT and 600 °C to derive the YS ratio (600 °C/RT). For the structural durability assessment, the fracture toughness was measured using the Charpy impact test. The key conclusions of this study are as follows.

(1) When more rolling passes were conducted below $T_{nr}$, the bainite fraction progressively decreased, whereas the ferrite fraction increased. Nb primarily existed in solid solution, with only a small portion forming fine precipitates or clusters. Although the PAGS of bainite was significantly refined from 33.91 to 18.14 μm, the substructure grain size (approximately 1.47 μm) and ferrite grain size (approximately 7.19 μm) remained nearly unchanged.
(2) With the increasing number of rolling passes conducted below $T_{nr}$, the tensile strength at RT remained nearly constant (~700 MPa), while the YS at both RT and 600 °C decreased gradually. Accordingly, the YS ratio (600 °C/RT) decreased from 0.717 to 0.501. In contrast, Charpy impact energy increased significantly from 32.9 J to 169.5 J, reflecting a substantial improvement in fracture toughness. These results clearly demonstrate the trade-off between strength and toughness induced by TMCP.
(3) Quantitative phase analysis based on EBSD maps using a KAM threshold ($K_{max} = 0.7^o$) confirmed that the bainite fraction decreased systematically from 79.28 % in TM70 to 26.99 % in TM16, validating the microstructural transition.
(4) Bainite fraction showed a strong linear correlation with the YS at both room and elevated temperatures, as well as with the YS ratio, indicating the critical role of bainite in high-temperature strength retention, and thus, fire resistance. In contrast, the improvement in fracture toughness was predominantly attributed to the increase in ferrite fraction, whereas bainite grain refinement played a complementary role.

These findings demonstrate the significance of microstructure-based process control in optimizing the strength-toughness balance. In particular, this study provides scientific evidence that fire resistance and fracture toughness can be effectively controlled through process optimization, laying a foundation for future research to maximize the mechanical performance through TMCP design.

## Declaration of competing interest

The authors declare that they have no known competing financial interests or personal relationships that could have appeared to influence the work reported in this paper.

## Acknowledgement

This study was financially supported by the Ministry of Trade, Industry, and Energy (Grant No. 20010453).

## Appendix A. Supplementary data

Supplementary data to this article can be found online at https://doi.org/10.1016/j.jmrt.2025.07.034.

## References

[1] Chijiiwa R, Yoshida Y, Uemori R, Tamehiro H, Funato K, Horii Y. Nippon Steel Tech Rep 1993;58:47–55. https://kyushu-u.elsevierpure.com/en/publications/development-and-practical-application-of-fire-resistant-steel-for-2.
[2] Kelly F, Sha W. J Constr Steel Res 1999;50(3):223–33. https://doi.org/10.1016/S0143-974X(98)00252-1.
[3] Sha W, Kirby BR, Kelly FS. Mater Trans 2001;42(9):1913–27. https://doi.org/10.2320/matertrans.42.1913.
[4] Panigrahi BK. Bull Mater Sci 2006;29:59–66. https://doi.org/10.1007/BF02709357.
[5] Speer J, Matlock D, Jansto S. Nb-microalloyed "Fire-Resistant" construction steels: recent progress. Proceedings of the value-added niobium microalloyed construction steels symposium CBMM and. Singapore: TMS; 2012. p. 5–7.

[6] Lee W-B, Hong S-G, Park C-G, Park S-H. Metall Mater Trans A 2002;33:1689–98. https://doi.org/10.1007/s11661-002-0178-2.
[7] Yoshida S, Okumura T, Kita H, Takahashi J, Ushioda K. Mater Trans 2014;55(6):899–906. https://doi.org/10.2320/matertrans.M2013393.
[8] Jo H-H, Shin C, Moon J, Jang JH, Ha H-Y, Park S-J, Lee T-H, Lee BH, Chung J-H, Speer JG. Mater Des 2020;194:108882. https://doi.org/10.1016/j.matdes.2020.108882.
[9] Wan R, Sun F, Zhang L, Shan A. Mater Des 2012;35:335–41. https://doi.org/10.1016/j.matdes.2011.09.009.
[10] Sim J-H, Kim T-Y, Kim J-Y, Kim C-W, Chung J-H, Moon J, Lee C-H, Hong H-U. Met Mater Int 2022;28:337–45. https://doi.org/10.1007/s12540-020-00870-y.
[11] Wan R, Sun F, Zhang L, Shan A. J Mater Eng Perform 2014;23:2780–6. https://doi.org/10.1007/s11665-014-1051-3.
[12] Moon J, Kim S-D, Lee C-H, Jo H-H, Hong H-U, Chung J-H, Lee BH. J Mater Res Technol 2021;15:5095–105. https://doi.org/10.1016/j.jmrt.2021.10.132.
[13] Li Z, Zhang K, Wang W, Wang X, Cao Y, Yong Q. Steel Res Int 2022;93(5):2100515. https://doi.org/10.1002/srin.202100515.
[14] Zhang Z, Niu G, Li J, Zhang P, Wu H. J Mater Eng Perform 2023;32(9):3958–67. https://doi.org/10.1007/s11665-022-07388-x.
[15] Yin C, Chen Z, Feng Y, Zhu W, Zhao Y, Chen L. J Mater Sci 2022;57(15):7706–18. https://doi.org/10.1007/s10853-022-07149-0.
[16] Ouchi C. ISIJ Int 2001;41(6):542–53. https://doi.org/10.2355/isijinternational.41.542.
[17] Tamura I, Sekine H, Tanaka T. Thermomechanical processing of high-strength low-alloy steels. Butterworth-Heinemann 2013.
[18] Vervynckt S, Verbeken K, Lopez B, Jonas J. Int Mater Rev 2012;57(4):187–207. https://doi.org/10.1179/1743280411Y.000000001.
[19] Akhtar MN, Khan M, Khan SA, Afzal A, Subbiah R, Ahmad SN, Husain M, Butt MM, Othman AR, Bakar EA. Mater 2021;14(10):2639. https://doi.org/10.3390/ma14102639.
[20] Mandalika BVR, Bonta SR, Soni RJ, Annamraju S, Nayaka N. J Mater Eng Perform 2024;33(4):1959–74. https://doi.org/10.1007/s11665-023-08110-1.
[21] Cong J, Li J, Fan J, Misra RDK, Xu X, Wang X. J Mater Res Technol 2021;13:1220–9. https://doi.org/10.1016/j.jmrt.2021.05.061.
[22] Uranga P, Shang C-J, Senuma T, Yang J-R, Guo A-M, Mohrbacher H. Adv Manuf 2020;8(1):15–34. https://doi.org/10.1007/s40436-019-00285-y.
[23] Zaefferer S, Romano P, Friedel F. J Microsc 2008;230(3):499–508. https://doi.org/10.1111/j.1365-2818.2008.02010.x.
[24] Jentner RM, Scholl S, Srivastava K, Best JP, Kirchlechner C, Dehm G. Mater Des 2023;236:112507. https://doi.org/10.1016/j.matdes.2023.112507.
[25] Kang J, Pottore NS, Zhu H, Tasan CC. Acta Mater 2023;254:118985. https://doi.org/10.1016/j.actamat.2023.118985.
[26] Niu W, Zhang X, Liang J, Shen Y, Xue W, Li J. J Mater Res Technol 2024;33:2331–42. https://doi.org/10.1016/j.jmrt.2024.09.230.
[27] Chen T, Cui E, Shen Y, Jia N, Wang Z, Fan Z. Mater Sci Eng, A 2024;901:146579. https://doi.org/10.1016/j.msea.2024.146579.
[28] Zhu K, Bouaziz O, Oberbillig C, Huang M. Mater Sci Eng, A 2010;527(24–25):6614–9. https://doi.org/10.1016/j.msea.2010.06.061.
[29] He S, He B, Zhu K, Huang M. Acta Mater 2017;135:382–9. https://doi.org/10.1016/j.actamat.2017.06.050.
[30] Fereiduni E, Banadkouki SG. J Alloys Compd 2013;577:351–9. https://doi.org/10.1016/j.jallcom.2013.05.209.
[31] Alibeyki M, Mirzadeh H, Najafi M, Kalhor A. J Mater Eng Perform 2017;26:2683–8. https://doi.org/10.1007/s11665-017-2687-6.
[32] Bhadeshia HKDH. Bainite in steels: theory and practice. 3rd. ed. 2015. London.
[33] Ym K, Yj L, Nj K. ISIJ Int 2002;42(12):1571–7. https://doi.org/10.2355/isijinternational.42.1571.
[34] Kaijalainen AJ, Suikkanen PP, Limnell TJ, Karjalainen LP, Kömi JI, Porter DA. J Alloys Compd 2013;577:S642–8. https://doi.org/10.1016/j.jallcom.2012.03.030.
[35] Escobar JD, Delfino P, Ariza-Echeverri EA, Carvalho F, Schell N, Stark A, Rodrigues T, Oliveira J, Avila J, Goldenstein H. Mater Char 2021;182:111567. https://doi.org/10.1016/j.matchar.2021.111567.
[36] Dong X, Shen Y, Zhu Y. Mater Res Lett 2023;11(1):69–75. https://doi.org/10.1080/21663831.2022.2116295.